Geosci. Instrum. Method. Data Syst., 5, 27–44, 2016
www.geosci-instrum-method-data-syst.net/5/27/2016/
doi:10.5194/gi-5-27-2016

Geoscientific Instrumentation Methods and Data Systems
Open Access

A compact receiver system for simultaneous measurements of mesospheric CO and O_3

P. Forkman[1], O. M. Christensen[1], P. Eriksson[1], B. Billade[1], V. Vassilev[2], and V. M. Shulga[3]

[1]Department of Earth and Space Sciences, Chalmers University of Technology, Gothenburg, Sweden
[2]Department of Microtechnology and Nanoscience, Chalmers University of Technology, Gothenburg, Sweden
[3]Institute of Radio Astronomy, Ukrainian Academy of Sciences, Kharkov, Ukraine

Correspondence to: P. Forkman (peter.forkman@chalmers.se)

Received: 18 June 2015 – Published in Geosci. Instrum. Method. Data Syst. Discuss.: 9 September 2015
Revised: 23 December 2015 – Accepted: 16 January 2016 – Published: 5 February 2016

Abstract. During the last decades, ground-based microwave radiometry has matured into an established remote sensing technique for measuring vertical profiles of a number of gases in the stratosphere and the mesosphere. Microwave radiometry is the only ground-based technique that can provide vertical profiles of gases in the upper stratosphere and mesosphere both day and night, and even during cloudy conditions. Except for microwave instruments placed at high-altitude sites, or at sites with dry atmospheric conditions, only molecules with significant emission lines below 150 GHz, such as CO, H_2O, and O_3, can be observed. Vertical profiles of these molecules can give important information about chemistry and dynamics in the middle atmosphere.

Today these measurements are performed at relatively few sites; more simple and reliable instrument solutions are required to make the measurement technique more widely spread. This need is urgent today as the number of satellite sensors observing the middle atmosphere is about to decrease drastically. In this study a compact double-sideband frequency-switched radiometer system for simultaneous observations of mesospheric CO at 115.27 GHz and O_3 at 110.84 GHz is presented.

The radiometer, its calibration scheme, and its observation method are presented. The retrieval procedure, including compensation of the different tropospheric attenuations at the two frequencies and error characterization, are also described. The first measurement series from October 2014 until April 2015 taken at the Onsala Space Observatory, OSO (57° N, 12° E), is analysed. The retrieved vertical profiles are compared with co-located CO and O_3 data from the MLS instrument on the Aura satellite. The data sets from the instruments agree well with each other. The main differences are the higher OSO volume mixing ratios of O_3 in the upper mesosphere during the winter nights and the higher OSO volume mixing ratios of CO in the mesosphere during the winter. The low bias of mesospheric winter values of CO from MLS compared to ground-based instruments was reported earlier.

1 Introduction

Simultaneous measurements of mesospheric gases with different chemical lifetimes, such as ozone (fraction of an hour) and carbon monoxide (order of weeks), can give important information on both chemical and dynamical processes in this altitude region. The middle atmospheric distribution of ozone, O_3, is characterized by a stratospheric volume mixing ratio (vmr) peak at ~ 35 km altitude, first described by Chapman (1930), and a diurnally varying secondary mesospheric peak at ~ 90 km altitude (Hays and Roble, 1973). The secondary peak is formed during night by reactions between atomic and molecular oxygen and partly destroyed by photo-dissociation during day. Additionally, a tertiary, also diurnally varying, peak is present at ~ 72 km in winter at high latitudes (Marsh et al., 2001; Hartogh et al., 2011).

The main source of middle atmospheric carbon monoxide, CO, is photo-dissociation of carbon dioxide, CO_2, in the upper mesosphere/thermosphere region. Reactions with hydroxyl, OH, are the main sink. A low vmr in the stratosphere, significantly increasing values with altitude up through the mesosphere, and high values in the thermosphere, is the typical vertical distribution of middle atmospheric CO (Lopez-Puertas et al., 2000).

The vertical component of the mesospheric dynamics can at high latitudes be described as an annual cycle with air ascending in the summer and descending in the winter. The horizontal component is weak during summer, while it is controlled by the polar vortex and is stronger during winter (Brasseur and Solomon, 2008). Due to its long lifetime in the mesosphere, CO is an excellent tracer of dynamics in this altitude region, especially at high latitudes during winter (Hoffmann, 2012).

Microwave radiometry is the only ground-based remote sensing technique that both day and night, even during cloud cover, can provide vertical profiles of different trace gases up to the mesopause region. In microwave radiometry, emission spectra from rotational transitions within the observed molecular species are measured. Due to pressure broadening, the measured spectra contain information about the vertical distribution of the molecule. Except from very dry sites, or sites at high altitudes, only frequencies up to about 150 GHz can be observed, since higher frequencies are effectively attenuated by tropospheric water (Janssen, 1993). The gases CO, H_2O, O_2, and O_3 all have sufficiently strong emissions at frequencies below 150 GHz. Thus, there is a need for simple and reliable radiometers operating below 150 GHz, since they can observe important gases from almost every ground-based site. If such a radiometer could also observe two of the gases simultaneously (e.g. O_3 and CO), it would be even more useful for the microwave community.

Dicke-switching is the generally used observation technique in microwave radiometry, meaning that the radiation from the sky is compared to an equally intense reference source to diminish the effects of gain variations. Three main Dicke-switching variants can be recognized. In load-switching the reference is a blackbody or other noise source. The zenith sky is the reference in sky-switching. In frequency-switching the mixer's local oscillator frequency, LO, is changed between the signal and the reference phases. Parrish (1994) gives an overview of the mentioned observation methods.

Since the pioneering work by Caton et al. (1968) several heterodyne radiometer systems dedicated to middle atmospheric O_3 observations have been developed, primarily for the relatively strong O_3 transitions at 110.8 and 142.2 GHz. Lobsiger (1987) developed a load-switching technique where the sky, a liquid nitrogen cold load at 80 K, and an ambient load were measured during each observation cycle; several 142.2 GHz instruments use variants of this method (Hartogh et al., 1991; Peter et al., 1998; Hocke et al., 2007; Palm et al., 2010; Moreira et al., 2015). Recently the technique has been developed further by implementing a noise diode and a Peltier cooled load (Fernandez et al., 2015).

Parrish et al. (1988, 1992) developed a sky-switching procedure at 110.8 GHz where the reference zenith beam passes a lossy window at a Brewster angle to compensate for the higher intensity in the signal beam. This observation technique has been widely used, for example by Connor et al. (1994), Boyd et al. (2007), and Nedoluha et al. (2015).

The drawback of load and sky switching is that a reference is observed during half the observation time. The advantage of frequency-switching is that the wanted sky emission is present in both signal and reference, which doubles the effective observation time compared to load or sky switching. The drawback is that the frequency-dependent impedances in the front-end components can change the overall gain between the signal and reference phases if the frequency throw is more than ~ 30 MHz. As the pressure broadening in the stratosphere exceeds the bandwidth limitation of frequency-switching, this method can only be used for studies of mesospheric and upper stratospheric O_3. However, narrow mesospheric lines can be resolved with a higher temporal resolution using a frequency-switched configuration compared to load or sky switching due to the efficient time usage. Nagahama et al. (1999) used a frequency throw of 30 MHz and presented vertical O_3 profiles in the altitude range 30–80 km.

Microwave spectra of CO are much narrower than spectra of O_3 due to the different residence altitudes for the two molecules, which make frequency-switching suitable. Waters et al. (1976) made the first microwave CO observations, using absorption measurements against the Sun and on-source off-source switching (the standard Dicke method used by radio astronomers). Kunzi and Carlson (1982), Aellig et al. (1995) and Forkman et al. (2003, 2012) made frequency-switched observations of CO at 115.3 GHz. de Zafra and Muscari (2004), Hoffmann et al. (2011) and Straub et al. (2013) used load-switching to observe CO at 230.5 GHz.

The mixer is the key component in the heterodyne radiometer. The incoming radio frequency, RF, is mixed with the LO, and the output intermediate frequency, IF, is a mix of the upper and lower sidebands. To avoid the unwanted sideband (or image band), the radiometer can be operated in single-sideband mode where the image band is suppressed before the mixing. If none of the sidebands is suppressed, we have a double-sideband system which makes it possible to observe signals from the two bands simultaneously. The disadvantages are that the sideband ratio has to be known and the tropospheric attenuation has to be corrected individually for the two bands if the tropospheric opacity differs between the two frequencies. Except for instruments where the LO is placed in the centre of the observed line, e.g. the 183 GHz water vapour radiometer for the ALMA project (Emrich et al., 2009), most ground-based radiometers today are single-sideband instruments. One exception is the 110–116 GHz radiometer for CO and O_3 observations designed and operated by Piddyachiy et al. (2010).

In this study we present the first simultaneous measurements of mesospheric O_3 at 110.8 GHz and CO at 115.3 GHz made by a ground-based, double-sideband and frequency-switched radiometer system. The system is operated at the Onsala Space Observatory, OSO (57.4° N, 11.9° E). The in-

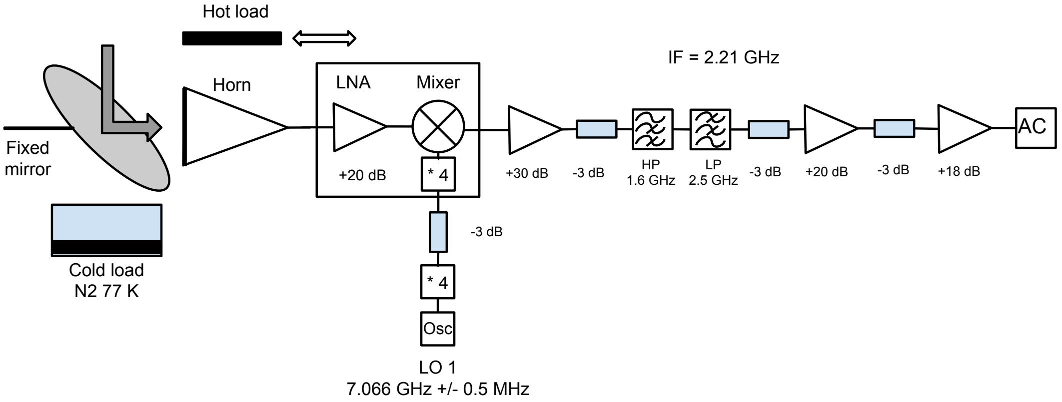

Figure 1. Block diagram of the DSB 110–115 GHz O_3/CO receiver system. The cold load is regularly mounted and used.

strument, its calibration scheme, the retrieval procedure and the first results are introduced. Section 2 describes the receiver system and the calibration and Sect. 3 presents the inversions. The results are given in Sect. 4 and the error analysis is described in Sect. 5. Section 6 shows a satellite comparison, and Sect. 7 gives a summary and the conclusions.

2 Instrument and observation technique

We present a double-sideband, frequency-switched heterodyne receiver system for simultaneous spectral measurements of the atmospheric O_3 $6_{15} \rightarrow 6_{06}$ transition at 110.836 GHz and the CO $1 \rightarrow 0$ transition at 115.271 GHz. Model calculations show that the highest signal to noise ratios of the observed mesospheric emission from both CO and O_3 are found at observation elevations larger than $\approx 40°$. To avoid Doppler shift effects due to zonal winds in the middle atmosphere an elevation as close to the zenith direction as possible is preferable. To get close to zenith but to avoid reflections from the housing structure an elevation of 80° was chosen. A 2-bit autocorrelator is used as a back-end spectrometer. The bandwidth is 20 MHz and the nominal resolution is 25 kHz (800 delay channels). This resolution is sufficient as the smallest line widths expected from the CO and O_3 line measured due to Doppler broadening have full width, half maximum values of 220 and 160 kHz respectively. A block diagram of the receiver is shown in Fig. 1 and technical specifications are given in Table 1.

2.1 Front-end description

The receiver front end includes a four-stage low-noise amplifier, LNA, a fundamental resistive mixer, and a $\times 4$ LO chain, all integrated onto a single monolithic microwave integrated circuit, MMIC, using a 100 nm mHEMT process. The mixer provides a conversion loss of 8–10 dB for LO power of 4 dBm. The LO chain consists of two doublers followed by a two-stage power amplifier. The amplifier delivers about 5 dBm of LO signal to the mixer with an input power of 9 dBm at 29.5 GHz. Vassilev et al. (2010) gives more details on the performance of the receiver and a description of the LNA.

Table 1. Receiver specifications.

Radio frequency	110–116 GHz, DSB
Mirror edge taper	-35 dB
Elevation	80°, fixed
Horn	Aluminium, corrugated
Full width half maximum	6°
First stage	LNA +20 dB, ambient temperature
Image sideband rejection	None, DSB
Sideband response	$0.50/0.50 \pm 0.05$
Local oscillator (LO)	Synth. + multipliers
LO frequency	113 GHz
Frequency throw ($2\Delta f$)	8 MHz
Mixer IF	2.21 GHz
DSB receiver temperature	~ 450 K
Back-end spectrometer	800 channel autocorrelator
Bandwidth	20 MHz
Nominal resolution	25 kHz
Integration time	6 h centered at 05:00, 11:00, 17:00, and 23:00 UTC

2.2 Calibration

Brightness temperature, T_b, derived from the Rayleigh–Jeans approximation of the Planck law, is often used as a measure of the received radiation in microwave radiometry. The Rayleigh–Jeans approximation can be written as

$$B(\lambda, T) \approx \frac{2kT}{\lambda^2}, \quad (1)$$

where B is the brightness describing the energy emitted by a black body, λ the wavelength, k the Boltzmann constant, and

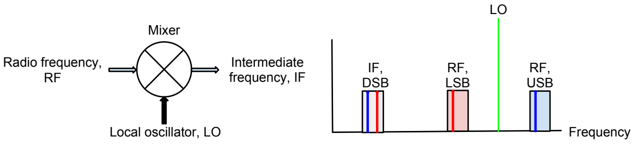

Figure 2. Mixer fundamentals.

T the physical temperature of the black body. Equation (1) is valid when $h\nu \ll kT$, where h is the Planck constant and ν is the frequency. The brightness temperature, T_b, is defined as

$$T_\mathrm{b} = I(\lambda)\frac{\lambda^2}{2k}. \tag{2}$$

The proportionality between the received radiation, I, and T_b is the reason why T_b is used in microwave radiometry. The antenna temperature, T_a, is defined as the convolution between the observed brightness temperature distribution and the antenna pattern. In the rest of this section a pencil beam is assumed, implying that the measured antenna temperature, T_a, is equal to the brightness temperature, T_b, in the observed direction.

The system temperature, the radiometer output power measured by the spectrometer, is defined as $T_\mathrm{sys} = T_\mathrm{a} + T_\mathrm{rec}$, where the receiver temperature, T_rec, is a measure of the power generated in the components along the radiometer system transmission line where the first stages as LNA and mixer contribute the most.

In the mixer, the RF input spectrum is folded around the LO to form the IF output spectrum (see Fig. 2). The IF bandpass filter selects the position and width of both the lower sideband, LSB, and the upper sideband, USB. If any of the two sidebands are terminated ahead of the mixer, the receiver is called single-sideband, SSB. We use the mixer in true double-sideband mode, DSB, where LSB is centered at 110.84 GHz and USB at 115.27 GHz; see the simulated spectra in Fig. 3. The contributions from LSB and USB are weighted with their relative front-end gains and then added to form T_sys (Ulich and Haas, 1976). The system temperature of a calibration blackbody load that fills the antenna beam, T_sys(load), can thus be expressed as

$$T_\mathrm{sys}(\mathrm{load}) = G_\mathrm{L}\left(T_\mathrm{load}(L) + T_\mathrm{rec}(L)\right) + G_\mathrm{U}\left(T_\mathrm{load}(U) + T_\mathrm{rec}(U)\right), \tag{3}$$

where L and U mark the contributions from the LSB and USB frequencies, G_L and G_U are the normalized relative front-end power gains ($G_\mathrm{L} + G_\mathrm{U} = 1$) in the two sidebands (also called sideband responses), and T_load is the temperature of the blackbody load. The sum of the two contributions to the receiver temperature is denoted T_rec, i.e. $T_\mathrm{rec} = G_\mathrm{L}\,T_\mathrm{rec}(L) + G_\mathrm{U}\,T_\mathrm{rec}(U)$. If it is assumed that the load is a blackbody in both sidebands, Eq. (3) is hence simplified to

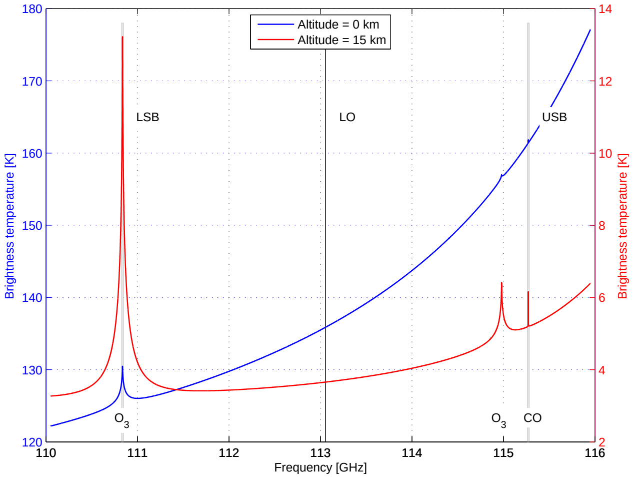

Figure 3. Simulated atmospheric spectra as seen with an elevation of 80° from the ground (blue) and, for clarity, from an altitude of 15 km (red). The 20 MHz wide LSB and USB frequency ranges and the LO frequency are marked.

$$T_\mathrm{sys}(\mathrm{load}) = T_\mathrm{load} + T_\mathrm{rec}. \tag{4}$$

To estimate T_rec, two blackbody loads with physical temperatures T_hot (ambient load) and T_cold (77 K load) are observed each month. T_rec can then be estimated using

$$\frac{P_\mathrm{cold}}{P_\mathrm{hot} - P_\mathrm{cold}} = \frac{T_\mathrm{sys}(\mathrm{cold})}{T_\mathrm{sys}(\mathrm{hot}) - T_\mathrm{sys}(\mathrm{cold})} = \frac{T_\mathrm{cold} + T_\mathrm{rec}}{T_\mathrm{hot} - T_\mathrm{cold}}$$
$$\rightarrow T_\mathrm{rec} = P_\mathrm{cold}\frac{T_\mathrm{hot} - T_\mathrm{cold}}{P_\mathrm{hot} - P_\mathrm{cold}} - T_\mathrm{cold}, \tag{5}$$

which is the classical Y factor method, where P_hot and P_cold are the measured powers observing the two loads. The system temperature when observing the sky, T_sys(sky), is given by

$$T_\mathrm{sys}(\mathrm{sky}) = G_\mathrm{L}T_\mathrm{a}(L) + G_\mathrm{U}T_\mathrm{a}(U) + T_\mathrm{rec}, \tag{6}$$

where $T_\mathrm{a}(L)$ and $T_\mathrm{a}(U)$ are the antenna temperatures at 110.84 and 115.27 GHz respectively.

The following calibration procedure is performed every 15 min to estimate the sky brightness temperature:

$$\frac{P_\mathrm{load} - P_\mathrm{sky}}{P_\mathrm{sky}} = \frac{T_\mathrm{sys}(\mathrm{load}) - T_\mathrm{sys}(\mathrm{sky})}{T_\mathrm{sys}(\mathrm{sky})}$$
$$= \frac{(T_\mathrm{load} + T_\mathrm{rec}) - (G_\mathrm{L}T_\mathrm{a}(L) + G_\mathrm{U}T_\mathrm{a}(U) + T_\mathrm{rec})}{G_\mathrm{L}T_\mathrm{a}(L) + G_\mathrm{U}T_\mathrm{a}(U) + T_\mathrm{rec}}, \tag{7}$$

where P_load and P_sky are the measured powers observing the load and the sky respectively. The weighted mean of the antenna temperatures at the two sidebands,

$$T_\mathrm{sky} = G_\mathrm{L}T_\mathrm{a}(L) + G_\mathrm{U}T_\mathrm{a}(U), \tag{8}$$

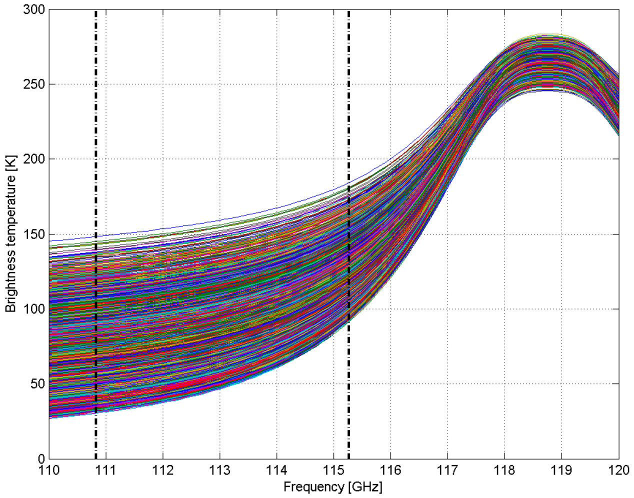

Figure 4. Simulated atmospheric spectra from 1 year of radiosonde data taken at the Landvetter airport 38 km NE of the Onsala site. Different tropospheric conditions explain the seen variation.

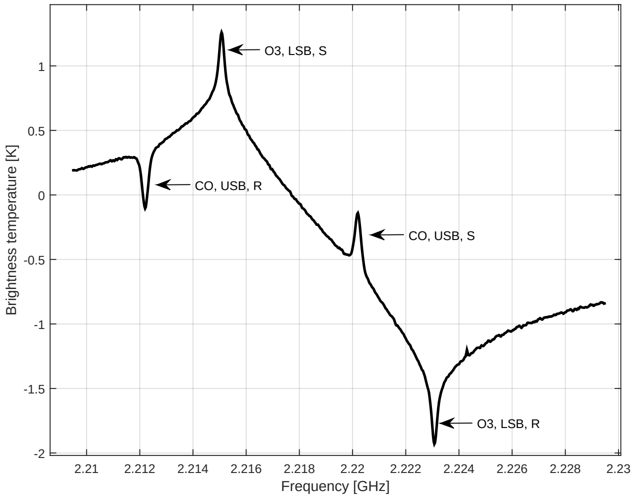

Figure 5. Average frequency-switched spectrum from December 2014 of O_3 from the lower sideband, LSB, and CO from the upper sideband, USB. S and R are the frequency-switching signal and reference phases. The wide wings of the O_3 line explain the general baseline shape.

can be derived from Eq. (7) since T_{load} and T_{rec} are known. Since a pencil beam is assumed, T_{sky} is denoted as sky brightness temperature (see above). An error in the estimate of T_{rec} introduces an error in the estimation of T_{sky}. The hot–cold calibrations (Eq. 5) performed so far indicate that the variation in T_{rec} is less than 3 %. Equations (7) and (8) then show that the error in T_{sky} is less than 2 %.

The sky brightness temperature at 115.3 GHz is 35–60 K higher than at 110.8 GHz. This is explained both by the frequency variation of absorption due to tropospheric water and by the fact that 115.3 GHz is situated higher on the wing of the 118 GHz O_2 line; see the broadband spectra in Fig. 4 estimated from 1 year of radiosonde data taken at Landvetter Airport, 38 km NE of Onsala Space Observatory.

2.3 Frequency-switching

The particular Dicke-switch method used here is frequency-switching. In this method the front-end mixer LO frequency, f_{LO}, is switched between the phases of the signal, S, and the reference, R, in the measurement cycle. $f_{\mathrm{LO}}(S) = f_c - \Delta f$ and $f_{\mathrm{LO}}(R) = f_c + \Delta f$ where f_c is the mean of the two local oscillator frequencies. Owing to $S - R$ being a difference, the spectra will show both a negative and a positive peak in the observed spectral characteristic, with a separation equal to the frequency throw, $2\Delta f$. An averaged spectrum is seen in Fig. 5. The spectrum is a combination of double-sideband measurement and frequency-switching, which explains the positions of the negative and positive peaks of O_3 from the lower sideband and CO from the upper sideband.

Using frequency-switching during the observation cycle, we record

$$\begin{aligned}\Delta T_{\mathrm{sky}} = {} & \frac{\Delta P}{P_{\mathrm{load}} - P_{\mathrm{sky}}}\left(T_{\mathrm{load}} - T_{\mathrm{sky}}\right) = T_{\mathrm{sky}}(-\Delta f) \\ & - T_{\mathrm{sky}}(+\Delta f) = G_{\mathrm{L}}\left(T_{\mathrm{a}}(L, -\Delta f) - T_{\mathrm{a}}(L, +\Delta f)\right) \\ & + G_{\mathrm{U}}\left(T_{\mathrm{a}}(U, -\Delta f) - T_{\mathrm{a}}(U, +\Delta f)\right), \qquad (9)\end{aligned}$$

where ΔT_{sky} is the difference in brightness temperatures (since we assume a pencil beam) and $\Delta P = P_{\mathrm{S}} - P_{\mathrm{R}}$ is the difference in the measured powers between the two frequencies $f_{\mathrm{LO}}(S)$ and $f_{\mathrm{LO}}(R)$. The calibration procedure gives P_{load}, P_{sky}, T_{load}, and T_{sky}.

2.4 Sideband ratio

The sideband responses G_{L} and G_{U} have to be known accurately to be able to retrieve vertical profiles from the measured spectra. The measurement of the sideband responses relies on inserting a continuous wave (CW) of known amplitude in the RF path of the instrument and on measuring the down converted IF signal. The measurement is then repeated over several RF/IF frequencies to get the overall sideband response.

Figure 6 shows the set-up used for the measurement of the sideband response of the instrument. A mm-wave source generates a CW in the 110.5–115.5 GHz frequency band. A mm-wave spectrum analyser extender measures the amplitude of the CW signal. The radiometer front end and a spectrum analyser measure the amplitude of the down converted IF. All the measurement equipments are synchronized to a common reference clock.

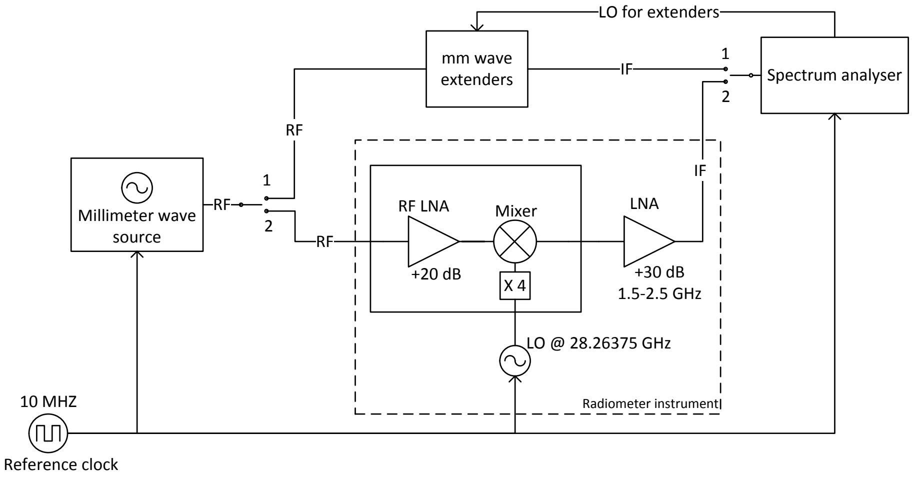

Figure 6. Set-up for sideband ratio measurement.

In the current measurement set-up, the mm-wave source is first connected to the extenders to measure the amplitude of the CW signal while sweeping the source frequency $f_{\mathrm{RF}} = 110.5 \rightarrow 115.5\,\mathrm{GHz}$. After taking the RF power sweep, the CW source is connected to the radiometer, and the amplitude of the down converted IF is recorded while sweeping the RF frequency as before. The local oscillator frequency of the radiometer is held constant at $f_{\mathrm{LO}} = 113.055\,\mathrm{GHz}$ (28.26375×4). The two sidebands after the IF amplifier bandpass response are

$$f_{\mathrm{LSB}} = 113.055 - (1.5 \rightarrow 2.5) = 110.555 \rightarrow 111.555\,\mathrm{GHz},$$
$$f_{\mathrm{USB}} = 113.055 + (1.5 \rightarrow 2.5) = 114.555 \rightarrow 115.555\,\mathrm{GHz}. \quad (10)$$

The sideband gains of the instrument can then be estimated by taking the ratios of the measured power at RF frequencies and IF frequencies as

$$g_{\mathrm{LSB}} = \frac{P_{\mathrm{IF}}^{\mathrm{LSB}}}{P_{\mathrm{RF}}^{\mathrm{LSB}}} \text{ and } g_{\mathrm{USB}} = \frac{P_{\mathrm{IF}}^{\mathrm{USB}}}{P_{\mathrm{RF}}^{\mathrm{USB}}}. \quad (11)$$

The measured sideband ratio, $g_{\mathrm{LSB}} / g_{\mathrm{USB}}$, is close to unity. However, standing-wave patterns are seen in both the measured RF and IF powers, which introduce an error in our estimation of the sideband ratio. These standing waves have to be minimized in order to improve the quality of the measurements. Nevertheless, the results obtained so far with the current set-up are promising. The linear normalized relative front-end power gains, $G_{\mathrm{L}} = g_{\mathrm{LSB}}/(g_{\mathrm{LSB}} + g_{\mathrm{USB}})$ and $G_{\mathrm{U}} = g_{\mathrm{USB}}/(g_{\mathrm{LSB}} + g_{\mathrm{USB}})$, are estimated at 0.5 ± 0.05 and 0.5 ± 0.05 respectively.

2.5 Water vapour radiometer for tropospheric measurements

Due to the nature of DSB mixers, the measured sky brightness temperature is the mean of the brightness temperatures at the lower and upper sideband frequencies, weighted with their respective sideband gains G_{L} and G_{U}. To be able to correct for the tropospheric attenuation, an estimation of the sky brightness temperatures at these two frequency regimes is needed. The OSO site operates two dual-frequency radiometers, ASTRID (Elgered and Jarlemark, 1998) and KONRAD (Stoew et al., 2000), that continuously measure the sky brightness temperature in different directions at 21.0/31.4 and 20.6/31.6 GHz respectively (see Table 2). The data are used to provide independent corrections for the water vapour induced time delay which affects the accuracy of the geodetic VLBI observations performed at the observatory (Elgered and Jarlemark, 1998). For our purpose, the calibrated zenith sky brightness temperatures from these instruments will be used in Sect. 3.3 to estimate the tropospheric opacity at 110.84 and 115.27 GHz.

3 Retrievals

3.1 Forward model

For the retrievals presented in this paper, the Atmospheric Radiative Transfer Simulator (ARTS v.2.3.145) is used as a forward model (Buehler et al., 2005; Eriksson et al., 2011). It is a general radiative transfer model that can provide Jacobians for a large number of different measurement geometries and systems. A 1-D simulation set-up is applied using a pressure grid ranging from 1.3×10^5 Pa (0 m) to 7.5×10^{-4} Pa (~ 130 km) with a spacing of ~ 250 m. Line-by-line simulations of frequencies in two bands between 110.816–110.856 and 115.251–115.291 GHz are run with a monochromatic frequency grid having a spacing of 4.2 MHz at the far end of each band, decreasing to 14.13 kHz in the centre of each band. The instrument is modelled as a dual-sideband receiver with a flat 50 % sideband response in each band. Each channel of the autocorrelator is modelled to have a channel response corresponding to an ideal Hanning filter

Table 2. Specifications for the total power dual channel radiometers.

Radiometer	ASTRID	KONRAD	Unit
Radio frequencies	21.0 / 31.4	20.6 / 31.6	(GHz)
Antenna (one for each frequency)	Dielectrically loaded horn	Conical lens horns	
Beam width, FWHM	6/6	2.9/2.0	(°)
Pointing resolution	0.1	0.1	(°)
Reference load temperatures	313/360	313/373	(K)
System noise temperature	450/550	450/550	(K)
RF bandwidth (both channels)	1000	320	(MHz)
Accuracy	< 1	0.5	(K)

with a FWHM of 50 kHz. The antenna is modelled as a pencil beam antenna looking at a zenith angle of 10°, and the instrument is positioned at ground level.

The spectroscopic lines included in the forward model are CO at 115.27 GHz, O_3 at 110.77, 110.84, 111.05, and 114.97 GHz, as well as complete absorption models for oxygen, nitrogen, water vapour, and liquid water (Table 3). The spectroscopic parameters are taken from an updated version of the Verdandi database (Eriksson and Merino, 1997). Line positions and strengths of the database are mainly taken from the JPL catalogue (Pickett et al., 1998), while the broadening parameters are mainly taken from HITRAN. The discussed version of Verdandi was created in 2002, using the JPL data of that time and HITRAN 2001 (Rothman et al., 2003). For a number of transitions the JPL and HITRAN data are replaced with hand-picked data from the literature. This includes the O_3 line at 110.84 GHz, where the pressure broadening parameters are taken from Connor and Radford (1986). A summary of the spectroscopic parameters is given in Table 4.

When comparing the measurements to a forward model simulation with the line positions from the JPL catalogue, the simulated CO emission occurs at the same frequency in both the simulation and our measurements, while the simulated O_3 line emission at 110.8360400 GHz shows a clear frequency offset compared to the measurements. Since the CO line is positioned correctly, a shift in the LO frequency cannot explain the frequency offset of the O_3 line. This indicates that the databases have the wrong frequency for this spectral line. Best agreement between the forward model and measurement was found if the line was shifted 117 kHz (the specified uncertainty is 50 kHz) to 110.8359230 GHz. Note that for the purpose of this study, the exact reason for this shift is not relevant, since a pure shift in frequency does not affect the retrieved concentrations as long as the modelled and measured spectra are consistent.

Table 3. Summary of the complete absorption models. The model name refers to the name used internally in ARTS, while the model is described in the reference given.

Species	Absorption model	Reference
N_2	N2-SelfContStandardType	Rosenkranz (1993)
O_2	O2-PWR98	Rosenkranz (1998)
H_2O	H2O-PWR98	Rosenkranz (1998)
Liquidwater	liquidcloud-MPM93	Liebe et al. (1993)

3.2 Retrieval model

To retrieve CO and O_3 concentrations from the measured spectra, the maximum a posteriori method, also called the optimal estimation method, OEM (Rodgers, 2000), is used as implemented in the updated version of the Qpack software (Eriksson et al., 2005). Given the spectra with assumed errors and a statistical distribution of the measured atmosphere, the method returns the maximum a posteriori estimate combining these two pieces of information. If the atmosphere and possible instrument parameters are described by a state vector $\boldsymbol{x}$, the measured spectrum by $\boldsymbol{y}$, and the a priori atmosphere by $\boldsymbol{x}_{\mathrm{a}}$, the estimated atmosphere is

$$\hat{\boldsymbol{x}} = \boldsymbol{x}_{\mathrm{a}} + \left(\mathbf{K}^T \mathbf{S}_{\epsilon^{-1}} \mathbf{K} + \mathbf{S}_{\mathrm{a}^{-1}}\right) \mathbf{K}^T \mathbf{S}_{\epsilon^{-1}} \left(\boldsymbol{y} - \mathbf{K}\boldsymbol{x}_{\mathrm{a}}\right), \qquad (12)$$

where $\mathbf{S}_\epsilon$ and $\mathbf{S}_{\mathrm{a}}$ are the covariance matrices describing the uncertainty (assuming normal distribution) in the measurements and a priori atmosphere respectively. The Jacobian or weighting function matrix, $\mathbf{K} \equiv \partial \boldsymbol{y} / \partial \boldsymbol{x}$, is the linearized derivative of the forward model and describes how a change in any of the state vector elements influences the measured spectrum. Tropospheric attenuation introduces a non-linearity in Eq. (12); i.e. $\mathbf{K}$ is a function of $\boldsymbol{x}$. To account for this, Eq. (12) is solved iteratively using a Gauss–Newton method, and convergence is considered to be reached when the change in the state vector between two iterations, normalized by the retrieved covariance, is less than 0.01 times the length of the state vector.

Table 4. Summary of the two major spectroscopic lines.

Line parameter	CO	O_3	Unit
Centre frequency, f_0	115.2712018	110.8359230	(GHz)
Line intensity, I_0	9.761128×10^{-18}	3.567796×10^{-17}	($\mathrm{m^2\,Hz^{-1}}$)
Ref. temp. for line intensity	300	300	(K)
Air broadened width	23332.68	23932.87	($\mathrm{Hz\,Pa^{-1}}$)
Self broadened width	25958.54	30009.87	($\mathrm{Hz\,Pa^{-1}}$)
Ref. temp. for broad. param.	296	296	(K)
Temp. dep. exp. for broad. param.	0.69	0.73	(–)

To save computational resources, the inverse problem (Eq. 12) is solved on a coarser grid than the forward model. The state vector is specified to contain the concentration of CO as a fraction of the a priori profile and the concentration of O_3 in vmr at pressure levels between 1×10^5 and 1×10^{-3} Pa with a spacing of 2 km. In addition to CO and O_3, the state vector includes the concentration (in units relative to the a priori profile) of water vapour and liquid water between 1×10^5 and 1.3×10^3 Pa with a spacing of 1 km. These species are included to correct for tropospheric influence on the mesospheric emission (see Sect. 3.3). The elements of the state vector containing these species are referred to as $\boldsymbol{x}^{\mathrm{trop}}$. To account for baseline ripple in the instrument, a third-order polynomial fit is performed, and its coefficients are stored in the last four elements of the state vector.

Each of these state vector variables needs a priori values stored in $\boldsymbol{x_a}$. The a priori profile for CO and O_3 is based on a climatology containing the monthly zonal mean values from ACE-FTS at 57.5° N. It is based on the method described in Jones et al. (2012) but with an updated data quality classification (Sheese et al., 2015). The climatology covers pressure levels from 1×10^5 to 1×10^{-4} Pa, but lacks data for certain months and altitudes. A linear interpolation between months is used if values are missing. Above 1×10^{-4} Pa the climatology is extrapolated using the vmr value from 1×10^{-4} Pa. The temperature, altitude and pressure relationship is, above 100 Pa, taken from a climatology based on the MSISE-90 model (Hedin, 1991), while below 5000 Pa it is based on the database for used tropospheric correction (see Sect. 3.3). Between 5000 and 100 Pa the temperatures are obtained by a linear interpolation between the two data sets.

To solve Eq. (12), $\mathbf{S}_\epsilon$ and $\mathbf{S}_\mathrm{a}$ must be specified. We describe these covariances with a standard deviation and a correlation function (see e.g. Christensen and Eriksson, 2013). For $\mathbf{S}_\epsilon$ the standard deviation is equal to the thermal noise estimated from the measurements (~ 0.07 K) and correlation between channels is modelled as a Gaussian correlation function with a correlation length equal to 1.6 channels. The specification of $\mathbf{S}_\mathrm{a}$ depends on which state vector variable the elements describe. The covariance of CO is described with a standard deviation equal to 100 % of the a priori profile. This large uncertainty is needed to ensure a reasonable sensitivity despite the low signal to noise ratio of the CO measurements. For O_3 the standard deviation is described simply as 4 ppmv for all altitudes, and for temperature it is set to 5 K for all altitudes. The correlation between altitudes is set to follow a linear correlation function with a correlation length of 8 km for both species and the temperature. Tropospheric water vapour has a standard deviation equal to 10 % of the a priori value and a linear correlation function with a correlation length of 8 km, while the liquid water has a standard deviation equal to 100 % of the a priori value, and no correlation between altitudes. The baseline fit has a standard deviation of 4 K for all coefficients.

3.3 Tropospheric correction

In order to accurately estimate the CO and O_3 concentrations in the mesosphere, the tropospheric attenuation needs to be accounted for. A common way of achieving this is to model the troposphere as a single layer, with an effective temperature and opacity, and to perform a correction of the observed spectra prior to performing the retrieval. For the DSB receiver the difference in the opacity between the two sidebands is too large for such an approach to work, and as such the troposphere needs to be included directly in the forward model. This is done in two steps. First an atmosphere is selected from a database of tropospheric scenarios. The atmosphere selected is the one minimizing the following cost function:

$$\chi^2 = \left(\boldsymbol{y}^{\mathrm{trop}} - f\left(\boldsymbol{x}^{\mathrm{trop}}\right)\right)^T \mathbf{S}_\epsilon^{\mathrm{trop}} \left(\boldsymbol{y}^{\mathrm{trop}} - f\left(\boldsymbol{x}^{\mathrm{trop}}\right)\right), \qquad (13)$$

where $\boldsymbol{y}^{\mathrm{trop}}$ are the measurements used for the tropospheric correction, $f(\boldsymbol{x}^{\mathrm{trop}})$ the radiance from the modelled troposphere and $\mathbf{S}_\epsilon^{\mathrm{trop}}$ the covariance matrix describing the measurement noise for the measurements used for the tropospheric retrieval. For the DSB instrument, $\boldsymbol{y}^{\mathrm{trop}}$ consists of two elements, the mean T_{sky} measured across all channels, $T_{\mathrm{sky}}^{\mathrm{mean}}$, and the ground temperature at OSO at the time of the measurement, T_{ground}, measured by the weather station at the site. Both values are averaged over the same time period as the spectral measurements. The second step is to expand $\boldsymbol{y}$ in Eq. (12) to include $\boldsymbol{y}^{\mathrm{trop}}$ and retrieve $\boldsymbol{x}^{\mathrm{trop}}$ with the OEM method, using the selected troposphere as the a priori tropo-

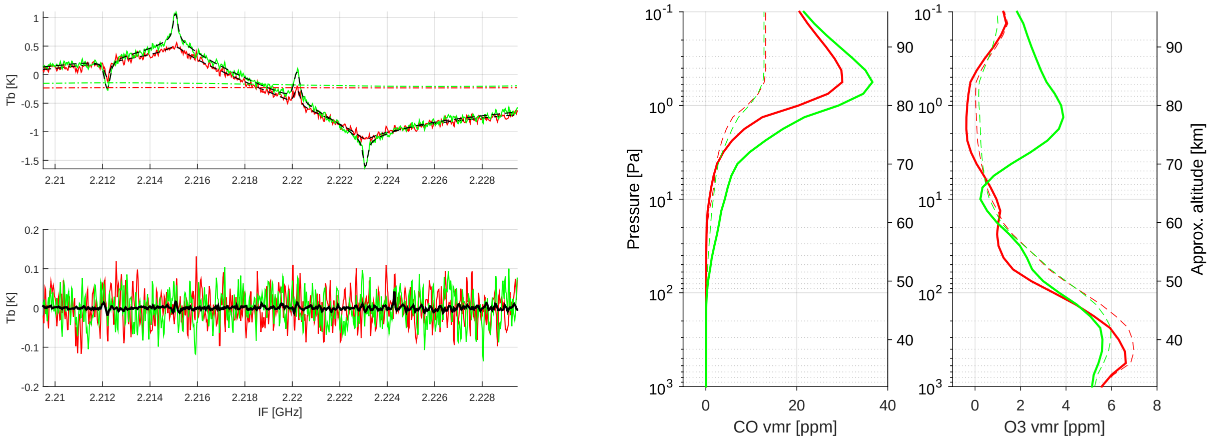

Figure 7. The top left panel shows measured spectra (solid lines) and fitted spectra (black-dashed lines) at two different times. The green line corresponds to a mid-winter night, while the red is an autumn day. The near-horizontal dashed-dotted lines are the fitted baselines for the two spectra. The lower left panel shows the residuals from the fitting of the two spectra together with the mean residual of all spectra (black line). The two right panels show the retrieved profiles for the corresponding cases, together with the a priori profile used (dashed).

sphere. The effect of tropospheric attenuation on the mesospheric spectra are thus also added to **K**.

The tropospheric states considered in Eq. (13) are taken from a database constructed of data from the ERA-Interim project (Dee et al., 2011), covering years 2009, 2010, and 2011. Data were extracted for the OSO site at 00:00 and 12:00 UTH each day of the 3-year long period. In total, the database contains 2190 atmospheric states. Temperature and humidity data were used as provided by ERA-Interim. The liquid water content, LWC, however, depends on the cloud cover and the distribution of clouds within a resolved grid cell in ERA-Interim. For the database used in this study, the liquid water content above OSO has been parameterized as a function of cloud fraction and mean liquid water content in an ERA-Interim grid box. The parameterization was corrected such that the fraction of cloudy to non-cloudy days and the maximum integrated liquid water path are consistent with measurements from ASTRID and KONRAD. Using this database, an a priori troposphere could be selected according to Eq. (13).

Fitting the troposphere using just $T_{\mathrm{sky}}^{\mathrm{mean}}$ and T_{ground} is a grossly under-determined problem, and thus to test the accuracy of this method the tropospheric attenuation was also simultaneously estimated by including measurements from water vapour radiometer ASTRID in $\boldsymbol{y}^{\mathrm{trop}}$ (averaged over the same time period as the double-sideband receiver). The two channels are simulated as described in Sect. 2.5 using the same settings as described in Sect. 3.1. Simulations were also run for KONRAD, and comparing the simulated brightness temperatures from the two water vapour radiometers and brightness temperature measured, an offset was seen. For clear sky days (i.e. no clouds) ASTRID systematically measured brightness temperatures 3 and 5 K lower than the simulations predicted for the lower and upper frequency channels respectively, while KONRAD had a bias of -2 and $+1$ K for the two channels. Since both radiometers differ in their bias, we assume that this discrepancy comes from instrumental errors. For the study presented in this paper, the ASTRID instrument alone is used to characterize possible errors in the tropospheric correction described by Eq. (13) (see Sect. 5). Thus, in order to ensure consistency between the simulations and the measurements, ASTRID was bias-corrected to match the simulated data before it is used.

4 Results of the OSO measurements

Figure 7 shows retrieved profiles from two example cases, one captured during a winter night and one during an autumn day. The winter spectrum shows stronger emission and less noise than the summer spectrum. The different noise levels mainly come from the higher tropospheric humidity in the autumn, leading to more attenuation of the mesospheric signal. Figure 8 shows all retrieved CO and O_3 from the measurement period. From the retrieved profiles, it is clear that stronger emission in the winter comes from an increase in CO and O_3 at altitudes above 10 Pa. The general structure of the CO distribution is seen in Fig. 8 with a sharp increase in volume mixing in the upper mesosphere.

This initial time series mainly covers the winter period. During the winter the general circulation brings down air from the thermosphere into the mesosphere, which increases the mesospheric CO abundance. This down-welling is strongest inside the polar vortex, and the variation of CO seen from day to day is mainly explained by movement of the polar vortex. OSO is sometimes located within and sometimes outside the vortex during the winter. During summer the general circulation is reversed and the abundance of CO in the mesosphere is reduced as air from the tropics and mid-

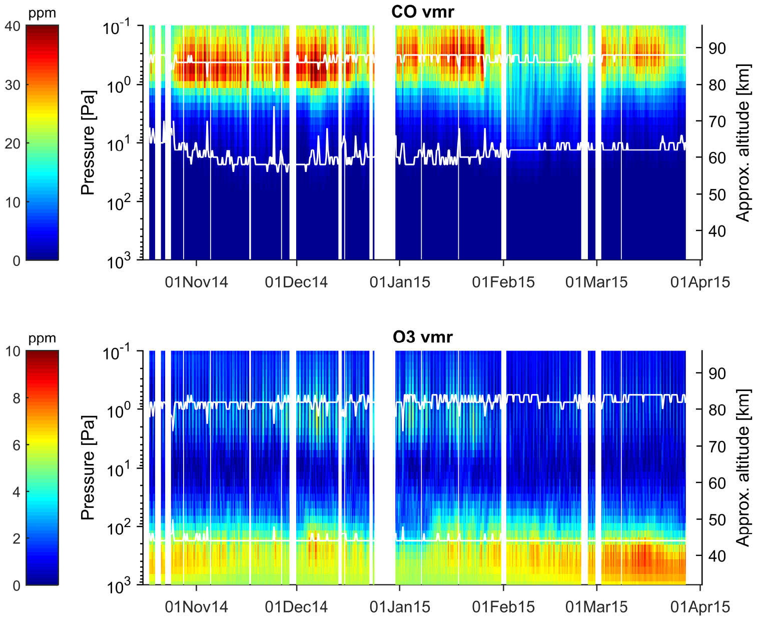

Figure 8. Retrieved vmr of CO and O_3 (ppm) for the measurement period. The white lines mark where the a priori profiles affects the result with 20 % (< 20 % between the lines).

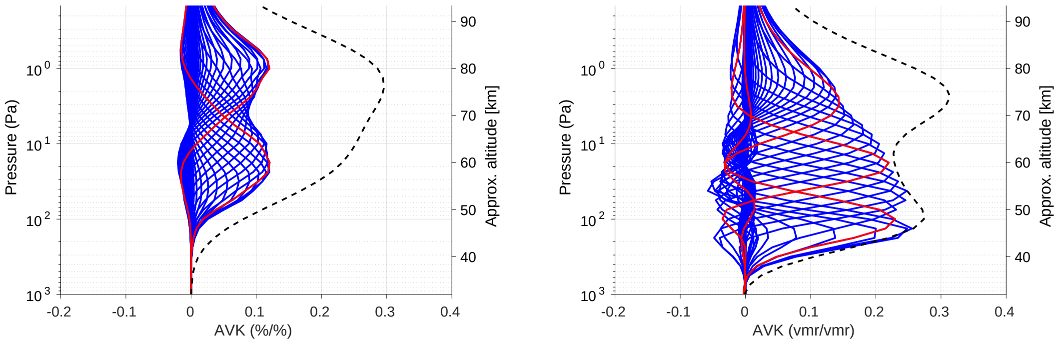

Figure 9. Averaging kernels for CO and O_3 for 16 November 2014. The kernels at 100, 18, 2.4 Pa for O_3 and 18, 1 Pa for CO are highlighted with red lines. The dashed line is the measurement response divided by 4.

latitudes is transported polewards in the lower mesosphere. This decrease in mesospheric CO can be seen at the end of our time series.

The time series of O_3 both show the upper part of the stratospheric peak and a nighttime peak at altitudes above 10 Pa during the winter. Due to the poor resolution of the instrument the observed mesospheric diurnal peak can be a mixture of both “the secondary ozone peak” at ∼ 90 km and “the tertiary ozone peak”, located at 72 km (see Sect. 1).

Example averaging kernels are shown in Fig. 9. For CO, the averaging kernels are shown with respect to a change in the atmosphere relative to the a priori profile, while for ozone the averaging kernels are shown with respect to vmr changes in the atmosphere. The reason for using different units for the two species is that for CO, large changes in terms of volume mixing ratio are more probable at high altitude than at lower. This strong vertical gradient of the CO concentration across the altitude range covered by the instrument must be accounted for in the retrieval procedure, and hence $\mathbf{S}_a$ is specified relative to the a priori profile. This in turn results in averaging kernels optimized with respect to such relative changes, and these averaging kernels are thus most descriptive of how the retrieved atmosphere changes with changes in the real atmosphere. The variability of O_3 around the a priori profile can be better represented with a constant vmr value, and hence averaging kernels with respect to this are shown.

The retrievals have a measurement response above 0.8 between 20 and 0.3 Pa for CO and between 200 and 0.8 Pa for O_3. Calculating the degrees of freedom of the retrievals (trace of the averaging kernel matrix), CO is retrieved with 1–2 degrees of freedom (depending on the season) and O_3 with 3–4.5 degrees of freedom, resulting in an average vertical res-

Table 5. Summary of the perturbations applied to the forward model and retrieval parameters in the sensitivity study. The method indicates how the perturbation values were estimated.

Parameter	Perturbation (1σ)	Method
Line strength (O_3/CO)	∼ 2 %	Comparison to HITRAN 2012
Pressure broadening parameter (O_3/CO)	10 %	Uncertainty given in HITRAN 2001
A priori profile	50 %	–
A priori uncertainty	50 %	–
Temperature profile	±5 K	1σ of MSISE-90 is 3 K.
Sideband response	5 %	Sect. 2.4
Tropospheric correction	Comparison to method using ASTRID	–

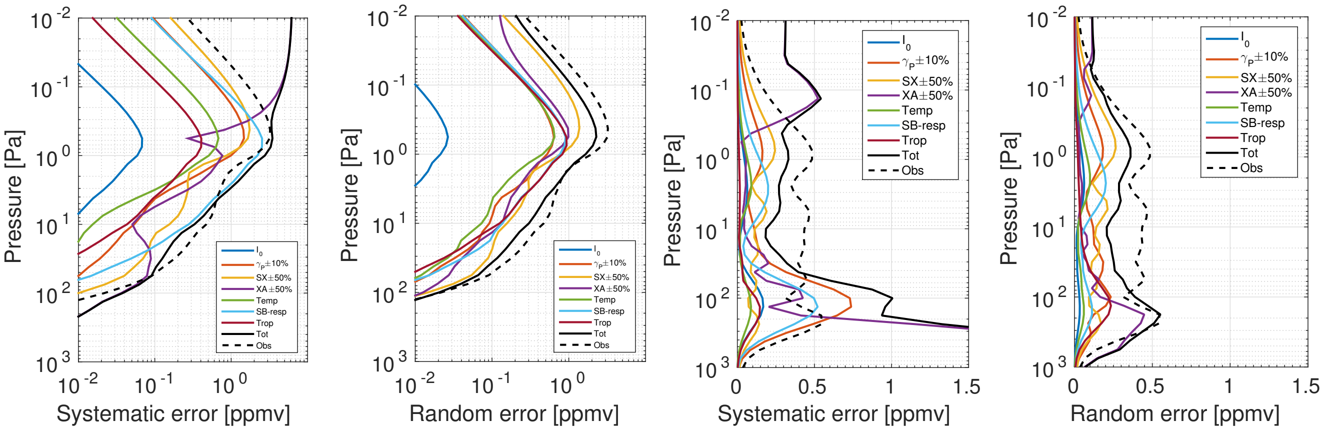

Figure 10. Estimated systematic and random errors for CO (two leftmost panels) and O_3 (two rightmost panels) estimated by perturbation of forward model and retrieval parameters. The parameters perturbed are line strength, I_0, pressure broadening parameter, γ_p, a priori variance, SX, a priori profile, XA, a priori temperature profile, Temp, the sideband response SB-resp, and the tropospheric correction Trop. The total RMSE (root mean square error) expected is given by the solid black line, and the observation error by the dashed black line.

olution of 20 and 10 km for CO and O_3 respectively. For altitudes above 70 km both lines are dominated by Doppler broadening, and thus retrieved values above this level may contain information from changes in the true atmosphere anywhere within this region. This is reflected by the fact that the averaging kernel for 2.4 and 1 Pa remains non-zero at the top of Fig. 9.

5 Sensitivity to errors in the forward model and retrieval parameters

Errors are introduced from uncertainties in the forward model and the retrieval parameters. These include uncertainties in the modelling of the instrument, uncertainties in the spectroscopic parameters used, uncertainties in the tropospheric correction, as well as a dependence on the a priori assumptions used in the retrievals. These errors introduce a bias in the mean atmospheric state retrieved, which we will describe as a systematic error. Additionally they add variability to the data which we will describe as a random error source, implying that it affects the scatter of the data set rather than the total mean.

To estimate these errors, the retrievals are rerun with each parameter perturbed with its 1-σ uncertainty. For the tropospheric correction the error was estimated by comparing the nominal correction method (using only $T_{\mathrm{sky}}^{\mathrm{mean}}$ and T_{ground}) to the extended tropospheric correction including ASTRID. The error estimation was carried out over the sub-set of measurements where simultaneous data from the OSO instrument and ASTRID were available (172 in total). For the spectroscopic parameters the uncertainty was estimated using either the difference between HITRAN 2012 and the value used in our retrieval or the 1-σ uncertainty reported in HITRAN 2001. The option leading to the greatest difference in the retrieved values was selected as a worst-case scenario. A summary of the values used is given in Table 5.

The mean difference (systematic errors) and the standard deviation (random errors) between each of the perturbed retrievals and the standard retrievals are shown in Fig. 10, together with the total root-sum-square error from all the parameters. For CO, the estimated systematic errors are around 0.2 ppmv for altitudes around 20 Pa, while degrading at altitudes above this, to 2.7 ppmv at 1 Pa. The largest source of systematic uncertainty is the characterization of the sideband

Table 6. Summary of error estimates.

Species	Pressure (Pa)	Systematic error (ppmv)	Random error (ppmv)
O_3	100	1.01	0.39
O_3	18	0.22	0.44
O_3	2.4	0.27	0.34
CO	18	0.18	0.19
CO	1	2.76	1.66

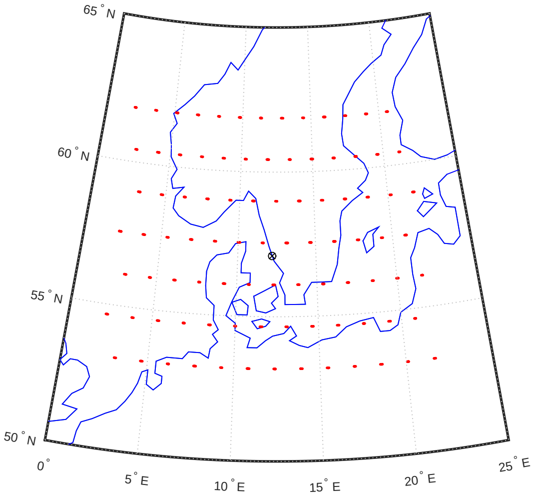

Figure 11. Collocations MLS-OSO.

response, followed by uncertainties in the a priori profile. The total estimated random errors for CO from the retrieval parameters are of the same size as the random error from thermal noise in the measurements (~ 0.2 ppmv at 20 Pa and ~ 3 ppmv at 1 Pa). For O_3, the estimated systematic and random errors from the simulated error sources are less than 0.5 ppmv between 50 and 1 Pa, with the largest source of systematic errors being uncertainties in the pressure broadening coefficient at low altitudes and the sideband response at high altitudes. Errors due to thermal noise in the measurements are better than 0.5 ppmv across all altitudes where the measurement response is greater than 0.8. A summary of estimated random and systematic errors for the retrieved data at example pressure levels is given in Table 6. For the estimate of the random errors, the maximum error from either thermal noise or forward model parameters is used.

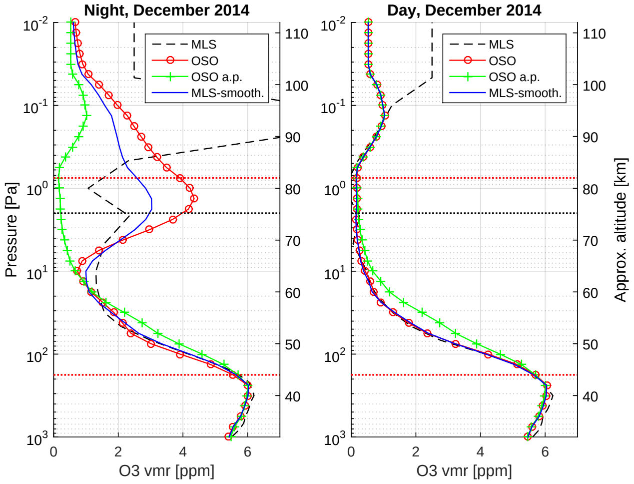

Figure 12. Average night and day vertical profiles of O_3 from December 2014. The a priori profile affects the OSO result < 20 % between the red dotted horizontal lines. The black dotted horizontal lines mark the upper altitude for the MLS data.

6 Satellite comparisons

The vertical profiles from the OSO instruments have been compared to version V-3-3 of CO and O_3 data from the microwave limb sounder (MLS) on the Aura satellite (Pumphrey et al., 2007; Froidevaux et al., 2008) (see Table 7). The comparison covers the time period October 2014 until April 2015. MLS data taken closer to the OSO site than latitude ±5° and longitude ±10° have been used (see Fig. 11). The MLS has measurements solely from either night (01:00–02:00 UTC) or day (11:00–12:00 UTC) within the used position range. Since the OSO data are 6 h averages, the 6 h period with the best overlap with the MLS measurement times has been used in the comparison. The MLS data were interpolated onto the OSO retrieval grid. To compensate for the different vertical resolution of the two instruments, the MLS data were convolved with the averaging kernels, A, of the OSO instrument (Rodgers and Connor, 2003):

$$\boldsymbol{x}_{\mathrm{s}} = \boldsymbol{x}_{\mathrm{a}} + \mathbf{A}\left(\boldsymbol{x}_{\mathrm{sat}} - \boldsymbol{x}_{\mathrm{a}}\right), \tag{14}$$

where $\boldsymbol{x}_{\mathrm{a}}$ is the OSO a priori profile and $\boldsymbol{x}_{\mathrm{s}}$ is the smoothed MLS profile.

Figures 12 and 14 show mean profiles of O_3 and CO for the two instruments. Figure 12 shows averaged night and day O_3 profiles from December 2014 and Fig. 13 shows the difference in vmr between OSO and MLS. The averaged day profiles from the two instrument are very similar within their measurement ranges. The night profiles however differ at altitudes above 5 Pa (~ 70 km), where OSO shows a more pronounced peak in the upper mesosphere. The MLS peak seen in the night profile at 2 Pa is probably “the tertiary ozone peak”.

There is no clear diurnal variation of the CO profiles. Figure 14 shows averaged day profiles from December 2014 and March 2015 and Fig. 15 shows the difference in vmr between OSO and MLS. OSO shows higher CO abundances than MLS at altitudes above 5 Pa during December. During March the difference between the two instruments is much less pronounced.

Table 7. Satellite characteristics.

Satellite instrument	Aura-MLS
Launch	15 July 2004
Orbit inclination	90°
Measurement principle	Limb sounding, emission
Frequency band	240 GHz
CO and O_3 versions	V-3-3
CO validation	Pumphrey et al. (2007)
O_3 validation	Froidevaux et al. (2008)
Vertical range	10–75 (85) km for O_3 (CO)
Vertical resolution (mesosphere)	7–8 km
Horizontal resolution (mesosphere)	200 km
Systematic errors (above 60 km)	$\sim \pm 20\,\%$
Co-location range satellite OSO	Lat. ±5° and long. ±10°
Co-located measurement days	140

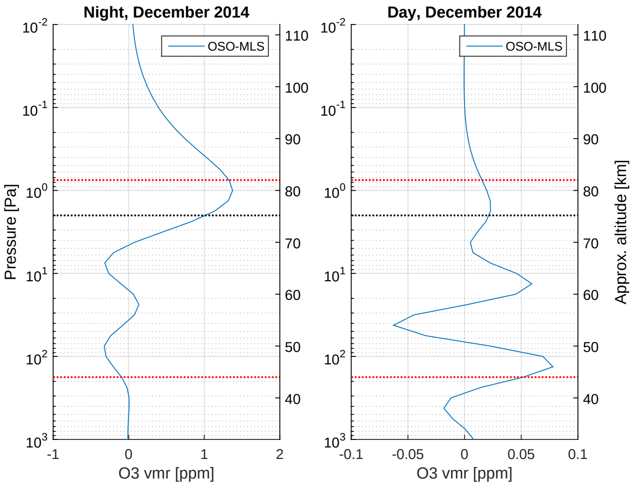

Figure 13. Difference between OSO and MLS (OSO-MLS) for night and day vertical profiles of O_3 from December 2014. The a priori profile affects the OSO result $< 20\,\%$ between the red dotted horizontal lines. The black dotted horizontal lines mark the upper altitude for the MLS data.

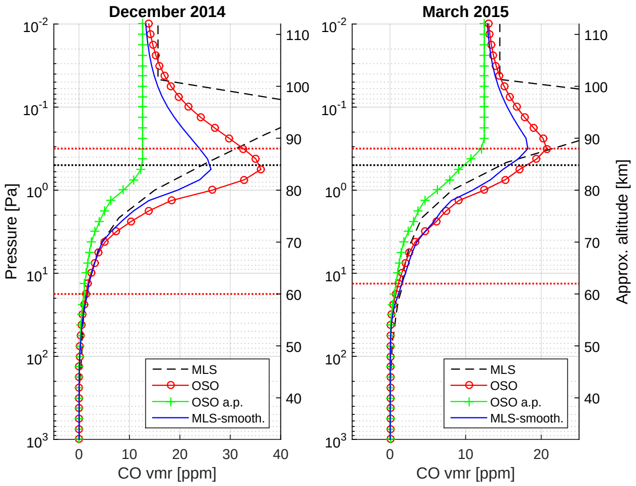

Figure 14. Average December and March vertical profiles of CO. The a priori profile affects the OSO result $< 20\,\%$ between the red dotted horizontal lines. The black dotted horizontal lines mark the upper altitude for the MLS data.

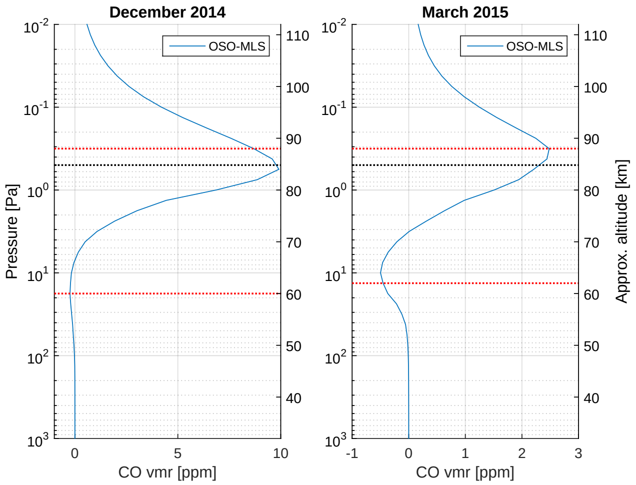

Figure 15. Difference between OSO and MLS (OSO-MLS) for December and March vertical profiles of CO. The a priori profile affects the OSO result $< 20\,\%$ between the red dotted horizontal lines. The black dotted horizontal lines mark the upper altitude for the MLS data.

Figures 16 and 17 show time series for the measurement period for OSO and the MLS at three different pressure levels (100, 18, and 2.4 Pa) for O_3 and at two different pressure levels (18 and 1 Pa) for CO. The average measurement response for OSO is higher than 80 % for both O_3 and CO at these pressure levels and the MLS reports valid mesospheric data at altitudes with pressures ≥ 2 Pa for O_3 and ≥ 1 Pa for CO. Note that due to the vertical resolution of the OSO instrument, the values at these pressure levels are not necessarily completely independent. The CO and O_3 data from the two instruments show the same general features, both in terms of the overall variation and in sporadic events. The main differences between the two instruments are both the higher OSO values of upper mesospheric O_3 mixing ratios during winter nights and the higher OSO values of upper mesospheric CO mixing ratios during the winter compared to the MLS (see also Figs. 12 and 14).

MLS data are often used for comparison with ground-based instruments. Boyd et al. (2007) (latitude $< 40°$) and Palm et al. (2010) (high latitudes) found good agreement between ground-based data sets of mesospheric daytime volume mixing ratios of O_3 compared to MLS. The nighttime values of Boyd et al. (2007) were also close to MLS; however, Palm et al. (2010) obtained higher O_3 mixing ratios above ≈ 70 km during winter nights. The "tertiary ozone peak" above ≈ 70 km is only present in winter nights at high

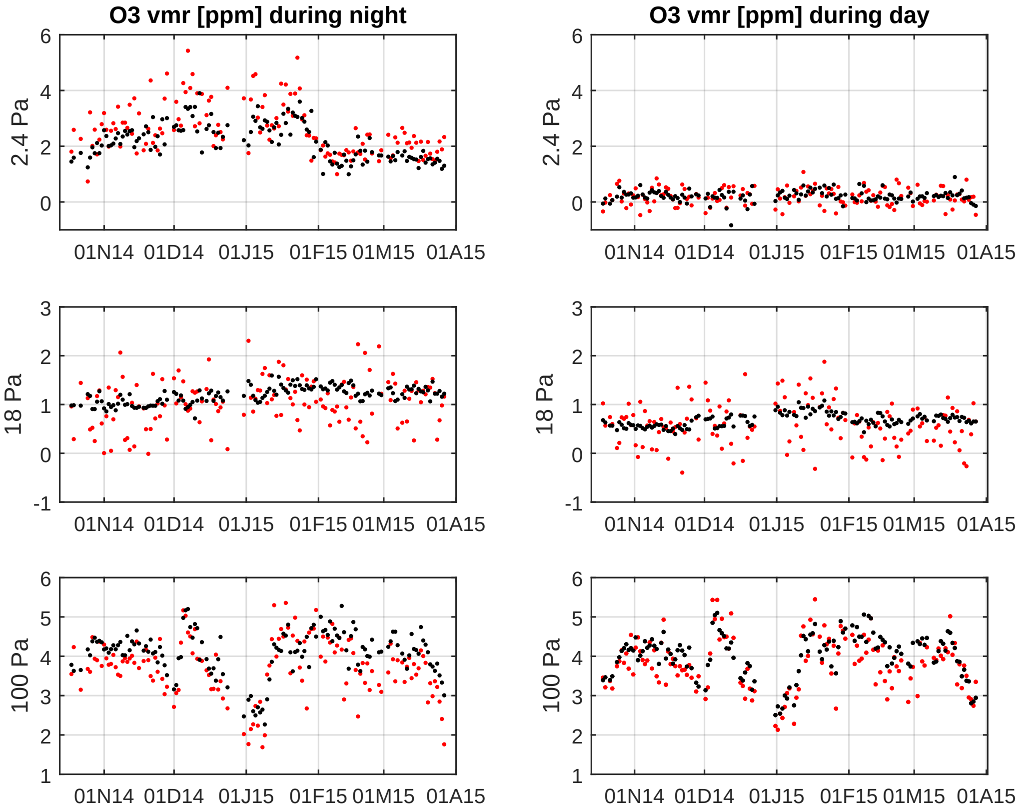

Figure 16. O_3 at three different altitudes, October–April (ddmyy), OSO (red), and MLS (black).

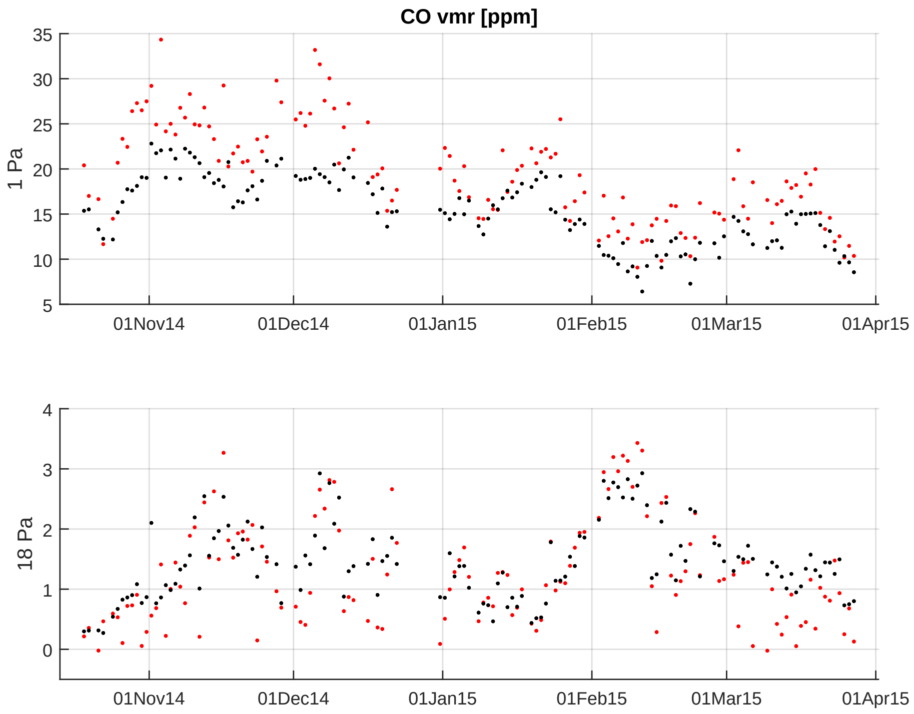

Figure 17. CO at two different altitudes, October–April (ddmmmyy), OSO (red), and MLS (black).

latitudes (Marsh et al., 2001) and can hence not be seen in the Boyd et al. (2007) data set. The altitude of the "tertiary ozone peak" is close to the upper limit of MLS O_3 data, which can explain the low bias of MLS winter nighttime O_3 above ≈ 70 km compared to the data presented in this report and to the data set of Palm et al. (2010).

Similar discrepancies between mesospheric CO measurements from MLS and ground-based instruments, as presented above, have been reported earlier by Forkman et al. (2012) using an older receiver system and by Hoffmann et al. (2011).

7 Summary and conclusions

The first simultaneous measurements of mesospheric O_3 at 110.8 GHz and CO at 115.3 GHz made by a ground-based, double-sideband, and frequency-switched radiometer system operated at the Onsala Space Observatory, OSO (57.4° N, 11.9° E), are presented.

Dicke-switching is the generally used observation method in microwave radiometry to diminish effects of gain variations in the receiver system. Frequency-switching is the most time-effective Dicke-switching variant since no reference load is observed except in the calibrations. Since the frequency throw has to be less than ~ 30 MHz to avoid gain differences, the method is restricted for studies of the spectral shapes of emission lines from high altitudes where the pressure broadening is limited. The method is hence well adapted for observations of mesospheric CO and O_3.

Most ground-based microwave heterodyne radiometers for atmospheric remote sensing are operated in single-sideband mode. In a double-sideband system simultaneous measurements of two emission lines at rather different frequencies, such as O_3 at 110.84 GHz and CO at 115.27 GHz, are possible. The drawbacks of a system where both sidebands are used are both that the sideband ratio has to be measured and that the tropospheric attenuation can differ between the two line frequencies.

In this study the gain between the front-end RF input and IF output was estimated by measuring the IF power when a calibrated RF source was connected to the front end. The RF source was swept across the lower and upper sidebands and the sideband ratio was estimated by comparing the IF and RF powers in the measured frequency range. Standing waves arising from reflections in the transmission line affect the result. In order to reduce the reported error in the sideband ratio estimation, the measurement set-up will be refined to try to diminish the standing waves.

The commonly used method to compensate measured spectra for the tropospheric attenuation is to use a one-layer model of the troposphere with constant effective temperature and opacity and to correct the observed spectra before the retrieval process. The difference between the opacities in the two sidebands is however too large for this method to work. An approach where the troposphere is included in the forward model has been used.

To calculate vertical profiles of CO and O_3 from the measured spectra, the optimal estimation method, OEM, has been used in the retrieval process. To present error estimations as exactly as possible, the systematic effects arising from the uncertainties in the different measurement and retrieval parameters have been carefully studied.

The OSO CO and O_3 data have been compared to measurements from the MLS satellite instrument (v3-3) on Aura. The data from two instruments show the same general features in both sporadic events and in the overall variation. The main differences between the instruments are the higher OSO values of O_3 mixing ratios in the upper mesosphere during the winter nights and the higher OSO winter values of CO mixing ratios in the upper mesosphere compared to MLS.

Microwave radiometry is the only ground-based remote sensing technique that can monitor the mesosphere day and night even during cloudy conditions. Simple and reliable microwave radiometers measuring in the frequency range below 150 GHz can be very valuable for mesospheric research since they can be operated at almost every ground-based site. The described instrument shows the potential of a double-sideband and frequency-switched radiometer system for simultaneous measurements of mesospheric CO and O_3.

Acknowledgements. The Swedish Natural Science Research Council supported the maintenance and development of the OSO receiver system. We thank the teams behind HITRAN and JPL for providing spectroscopic data to the retrievals. We thank the community behind ARTS for software used in the retrieval process and ECMWF for meteorological data, and Kaley Walker and Ja-Ho Koo for providing the climatology for CO and O_3 from the Atmospheric Chemistry Experiment (ACE). ACE, also known as SCISAT, is a Canadian-led mission mainly supported by the Canadian Space Agency and the Natural Sciences and Engineering Research Council of Canada. Finally we thank Rüdiger Haas for downloading and preparing of ERA-Interim data, and the laboratory and workshop of Onsala Space Observatory for keeping the OSO receiver up and running.

Edited by: F. Soldovieri

References

Aellig, C., Kaempfer, N., and Hauchecorne, A.: Variability of mesospheric CO in the fall and winter as observed with ground-based microwave radiometry at 115 GHz, J. Geophys. Res., 100, 14125–14130, doi:10.1029/95JD00984, 1995.

Boyd, I. S., Parrish, A. D., Froidevaux, L., Von Clarmann, T., Kyrölä, E., Russell, J. M., and Zawodny, J. M.: Ground-based microwave ozone radiometer measurements compared with Aura-MLS v2.2 and other instruments at two Network for Detection of Atmospheric Composition Change sites, J. Geophys. Res., 112, D24S33, doi:10.1029/2007JD008720, 2007.

Brasseur, G. and Solomon, S.: Aeronomy of the Middle Atmosphere, Springer-Verlag, Berlin, 2008.

Buehler, S. A., Eriksson, P., Kuhn, T., von Engeln, A., and Verdes, C.: ARTS, the Atmospheric Radiative Transfer Simulator, J. Quant. Spectrosc. Ra., 91, 65–93, doi:10.1016/j.jqsrt.2004.05.051, 2005.

Caton, W. M., Mannella, G. G., Kalaghan, P. M., Barrington, A. E., and Ewen, H. I.: Radio Measurement of the Atmospheric Ozone Transition at 101.7 GHz, Astrophys. J., 151, L153, doi:10.1086/180163, 1968.

Chapman, S.: A theory of upper-atmospheric ozone, Edward Stanford, in: Memoirs of the Royal Meteorological Society, Vol. 3, 103–125, http://www.rmets.org/sites/default/files/chapman-memoirs.pdf (last access: 3 February 2016), 1930.

Christensen, O. M. and Eriksson, P.: Time series inversion of spectra from ground-based radiometers, Atmos. Meas. Tech., 6, 1597–1609, doi:10.5194/amt-6-1597-2013, 2013.

Connor, B. J. and Radford, H.: Pressure broadening of millimeter-wave ozone lines by atmospheric gases, J. Mol. Spectrosc., 117, 15–29, doi:10.1016/0022-2852(86)90088-3, 1986.

Connor, B. J., Siskind, D. E., Tsou, J. J., Parrish, A., and Remsberg, E. E.: Ground-based microwave observations of ozone in the upper stratosphere and mesosphere, J. Geophys. Res., 99, 16757–16770, doi:10.1029/94JD01153, 1994.

Dee, D. P., Uppala, S. M., Simmons, A. J., Berrisford, P., Poli, P., Kobayashi, S., Andrae, U., Balmaseda, M. A., Balsamo, G., Bauer, P., Bechtold, P., Beljaars, A. C. M., van de Berg, L., Bidlot, J., Bormann, N., Delsol, C., Dragani, R., Fuentes, M., Geer, A. J., Haimberger, L., Healy, S. B., Hersbach, H., Hólm, E. V., Isaksen, L., Kållberg, P., Köhler, M., Matricardi, M., McNally, A. P., Monge-Sanz, B. M., Morcrette, J.-J., Park, B.-K., Peubey, C., de Rosnay, P., Tavolato, C., Thépaut, J.-N., and Vitart, F.: The ERA-Interim reanalysis: Configuration and performance of the data assimilation system, Q. J. Roy. Meteorol. Soc., 137, 553–597, doi:10.1002/qj.828, 2011.

de Zafra, R. L. and Muscari, G.: CO as an important high-altitude tracer of dynamics in the polar stratosphere and mesosphere, J. Geophys. Res, 109, D06105, doi:10.1029/2003JD004099, 2004.

Elgered, G. and Jarlemark, P. O. J.: Ground-based microwave radiometry and long-term observations of atmospheric water vapor, Radio Sci., 33, 707–717, doi:10.1029/98RS00488, 1998.

Emrich, A., Andersson, S., Wannerbratt, M., Sobis, P., Cherednichenko, S., Runesson, D., Ekebrand, T., Krus, M., Tegnader, C., and Krus, U.: Water Vapor Radiometer for ALMA, in: Twentieth International Symposium on Space Terahertz Technology, vol. 1, 174–177, www.nrao.edu/meetings/isstt/papers/2009/2009174177.pdf (last access: 3 February 2016), 2009.

Eriksson, P. and Merino, F.: On simulating passive observations of the middle atmosphere in the range 1–1000 GHz, Tech. rep., Chalmers University of Technology, Göteborg, Sweden, 1997.

Eriksson, P., Jiménez, C., and Buehler, S. A.: Qpack, a tool for instrument simulation and retrieval work, J. Quant. Spectrosc. Ra., 91, 47–64, doi:10.1016/j.jqsrt.2004.05.050, 2005.

Eriksson, P., Buehler, S. A., Davis, C. P., Emde, C., and Lemke, O.: ARTS, the atmospheric radiative transfer simulator, Version 2, J. Quant. Spectrosc. Ra., 112, 1551–1558, doi:10.1016/j.jqsrt.2011.03.001, 2011.

Fernandez, S., Murk, A., and Kämpfer, N.: GROMOS-C, a novel ground-based microwave radiometer for ozone measurement campaigns, Atmos. Meas. Tech., 8, 2649–2662, doi:10.5194/amt-8-2649-2015, 2015.

Forkman, P., Eriksson, P., Winnberg, A., Garcia, R., and Kinnison, D.: Longest continuous ground-based measurements of mesospheric CO, Geophys. Res. Lett., 30, 1532, doi:10.1029/2003GL016931, 2003.

Forkman, P., Christensen, O. M., Eriksson, P., Urban, J., and Funke, B.: Six years of mesospheric CO estimated from ground-based frequency-switched microwave radiometry at 57° N compared with satellite instruments, Atmos. Meas. Tech., 5, 2827–2841, doi:10.5194/amt-5-2827-2012, 2012.

Froidevaux, L., Jiang, Y. B., Lambert, A., Livesey, N. J., Read, W. G., Waters, J. W., Browell, E. V., Hair, J. W., Avery, M. A., McGee, T. J., Twigg, L. W., Sumnicht, G. K., Jucks, K. W., Margitan, J. J., Sen, B., Stachnik, R. A., Toon, G. C., Bernath, P. F., Boone, C. D., Walker, K. A., Filipiak, M. J., Harwood, R. S., Fuller, R. A., Manney, G. L., Schwartz, M. J., Daffer, W. H., Drouin, B. J., Cofield, R. E., Cuddy, D. T., Jarnot, R. F., Knosp, B. W., Perun, V. S., Snyder, W. V., Stek, P. C., Thurstans, R. P., and Wagner, P. A.: Validation of Aura Microwave Limb Sounder stratospheric ozone measurements, J. Geophys. Res., 113, D15S20, doi:10.1029/2007JD008771, 2008.

Hartogh, P., Hartmann, G., and Zimmerman, P.: Simultaneous Water Vapour And Ozone Measurements with Millimeterwaves In The Stratosphere And Mesosphere, in: Geoscience and Remote Sensing Symposium, 1991, IGARSS'91, vol. I, International Remote Sensing: Global Monitoring for Earth Management, Espoo, Finland, 227–230, doi:10.1109/IGARSS.1991.577719, 1991.

Hartogh, P., Jarchow, C., Sonnemann, G. R., and Grygalashvyly, M.: Ozone distribution in the middle latitude mesosphere as derived from microwave measurements at Lindau (51.66° N, 10.13° E), J. Geophys. Res., 116, D04305, doi:10.1029/2010JD014393, 2011.

Hays, P. and Roble, R. G.: Observation of mesospheric ozone at low latitudes, Planet. Space Sci., 21, 273–279, doi:10.1016/0032-0633(73)90011-1, 1973.

Hedin, A. E.: Extension of the MSIS thermosphere model into the middle and lower atmosphere, J. Geophys. Res., 96, 1159–1172, doi:10.1029/90JA02125, 1991.

Hocke, K., Kämpfer, N., Ruffieux, D., Froidevaux, L., Parrish, A., Boyd, I., von Clarmann, T., Steck, T., Timofeyev, Y. M., Polyakov, A. V., and Kyrölä, E.: Comparison and synergy of stratospheric ozone measurements by satellite limb sounders and the ground-based microwave radiometer SOMORA, Atmos. Chem. Phys., 7, 4117–4131, doi:10.5194/acp-7-4117-2007, 2007.

Hoffmann, C. G.: Application of CO as a tracer for dynamics in the polar winter middle atmosphere – A study based on ground-based microwave observations in Kiruna, PhD thesis, Universität Bremen, Bremen, http://elib.suub.uni-bremen.de/edocs/00102610-1.pdf (last access: 3 February 2016), 2012.

Hoffmann, C. G., Raffalski, U., Palm, M., Funke, B., Golchert, S. H. W., Hochschild, G., and Notholt, J.: Observation of strato-mesospheric CO above Kiruna with ground-based microwave radiometry – retrieval and satellite comparison, Atmos. Meas. Tech., 4, 2389–2408, doi:10.5194/amt-4-2389-2011, 2011.

Janssen, M. A.: Atmospheric Remote Sensing by Microwave Radiometry, John Wiley, New York, 1993.

Jones, A., Walker, K. A., Jin, J. J., Taylor, J. R., Boone, C. D., Bernath, P. F., Brohede, S., Manney, G. L., McLeod, S., Hughes, R., and Daffer, W. H.: Technical Note: A trace gas climatology derived from the Atmospheric Chemistry Experiment Fourier Transform Spectrometer (ACE-FTS) data set, Atmos. Chem. Phys., 12, 5207–5220, doi:10.5194/acp-12-5207-2012, 2012.

Kunzi, K. F. and Carlson, E. R.: Atmospheric CO volume mixing ratio profiles determined from ground-based measurements of the $J = 1 \rightarrow O$ and $J = 2 \rightarrow 1$ emission lines, J. Geophys. Res., 87, 7235–7241, doi:10.1029/JC087iC09p07235, 1982.

Liebe, H. J., Hufford, G. A., and Cotton, M. G.: Propagation modeling of moist air and suspended water/ice particles at frequencies below 1000 GHz, in: AGARD 52nd Specialists Meeting of the Electromagnetic Wave Propagation Panel, Palma de Mallorca, Spain, 1993.

Lobsiger, E.: Ground-based microwave radiometry to determine stratospheric and mesospheric ozone profiles, J. Atmos. Terr. Phys., 49, 493–501, doi:10.1016/0021-9169(87)90043-2, 1987.

Lopez-Puertas, M., Lopez-Valverde, M., Garcia, R., and Roble, R.: A review of CO_2 and CO abundances in the middle atmosphere, Geophys. Monogr., 123, 83–100, doi:10.1029/GM123p0083, 2000.

Marsh, D., Smith, A., Brasseur, G., Kaufmann, M., and Grossmann, K.: The existence of a tertiary ozone maximum in the high-latitude middle mesosphere, Geophys. Res. Lett., 28, 4531–4534, doi:10.1029/2001GL013791, 2001.

Moreira, L., Hocke, K., Eckert, E., von Clarmann, T., and Kämpfer, N.: Trend analysis of the 20-year time series of stratospheric ozone profiles observed by the GROMOS microwave radiometer at Bern, Atmos. Chem. Phys., 15, 10999–11009, doi:10.5194/acp-15-10999-2015, 2015.

Nagahama, T., Nakane, H., Fujinuma, Y., Ninomiya, M., Ogawa, H., and Fukui, Y.: Ground-based millimeter-wave observations of ozone in the upper stratosphere and mesosphere over Tsukuba, Earth Planets Space, 51, 1287–1296, doi:10.1186/BF03351602, 1999.

Nedoluha, G. E., Boyd, I. S., Parrish, A., Gomez, R. M., Allen, D. R., Froidevaux, L., Connor, B. J., and Querel, R. R.: Unusual stratospheric ozone anomalies observed in 22 years of measurements from Lauder, New Zealand, Atmos. Chem. Phys., 15, 6817–6826, doi:10.5194/acp-15-6817-2015, 2015.

Palm, M., Hoffmann, C. G., Golchert, S. H. W., and Notholt, J.: The ground-based MW radiometer OZORAM on Spitsbergen – description and status of stratospheric and mesospheric O_3-measurements, Atmos. Meas. Tech., 3, 1533–1545, doi:10.5194/amt-3-1533-2010, 2010.

Parrish, A.: Millimeter-wave remote sensing of ozone and trace constituents in the stratosphere, Proc. IEEE, 82, 1915–1929, doi:10.1109/5.338079, 1994.

Parrish, A., deZafra, R. L., Solomon, P. M., and Barrett, J. W.: A ground-based technique for millimeter wave spectroscopic observations of stratospheric trace constituents, Radio Sci., 23, 106–118, doi:10.1029/RS023i002p00106, 1988.

Parrish, A., Connor, B. J., Tsou, J. J., McDermid, I. S., and Chu, W. P.: Ground-based microwave monitoring of stratospheric ozone, J. Geophys. Res., 97, 2541–2546, doi:10.1029/91JD02914, 1992.

Peter, R., Caliseri, Y., and Kämpfer, N.: Variability of middle atmospheric ozone abundances derived from continuous ground-based millimeter wave measurements, in: Proceedings of the XVIII Quadrennial Ozone Symposium, L'Aquila, Italy, 559–562, 1998.

Pickett, H., Poynter, R., Cohen, E., Delitsky, M., Pearson, J., and Müller, H.: Submillimeter, millimeter, and microwave spectral line catalog, J. Quant. Spectrosc. Ra., 60, 883–890, doi:10.1016/S0022-4073(98)00091-0, 1998.

Piddyachiy, V., Shulga, V., Myshenko, V., Korolev, A., Myshenko, A., Antyufeyev, A., Poladich, A., and Shkodin, V.: 3-mm wave spectroradiometer for studies of atmospheric trace gases, Radiophys. Quantum Electron., 53, 326–333, doi:10.1007/s11141-010-9231-y, 2010.

Pumphrey, H. C., Filipiak, M., Livesey, N., Schwartz, M., Boone, C., Walker, K., Bernath, P., Ricaud, P., Barret, B., Clerbaux, C., Jarnot, R., Manney, G., and Waters, J.: Validation of middle-atmosphere carbon monoxide retrievals from MLS on Aura, J. Geophys. Res., 112, D24S38, doi:10.1029/2007JD008723, 2007.

Rodgers, C. D.: Inverse methods for atmospheric sounding: Theory and practice, World Scientific, Singapore, 2000.

Rodgers, C. D. and Connor, B.: Intercomparison of remote sounding instruments, J. Geophys. Res., 108, 4116, doi:10.1029/2002JD002299, 2003.

Rosenkranz, P. W.: Absorption of microwaves by atmospheric gases, in: Atmospheric remote sensing by microwave radiometry, edited by: Janssen, M. A., John Wiley & Sons Inc., New York, USA, 37–90, 1993.

Rosenkranz, P. W.: Water Vapor Microwave Continuum Absorption: A Comparison of Measurements and Models, Radio Sci., 33, 919–928, doi:10.1029/98RS01182, (correction in 34, 1025, 1999), 1998.

Rothman, L. S., Barbe, A., Chris Benner, D., Brown, L. R., Camy-Peyret, C., Carleer, M. R., Chance, K., Clerbaux, C., Dana, V., Devi, Fayt, A., Flaud, J.-M., Gamache, R. R., Goldman, A., Jacquemart, D., Jucks, K. W., Lafferty, W. J., Mandin, J.-Y., Massie, S. T., Nemtchinov, V., Newnham, D. A., Perrin, A., Rinsland, C. P., Schroeder, J., Smith, K. M., Smith, M. A. H., Tang, K., Toth, R. A., Vander Auwera, J., Varanasi, P., and Yoshino, K.: The HITRAN molecular spectroscopic database: edition of 2000 including updates through 2001, J. Quant. Spectrosc. Ra., 82, 5–44, doi:10.1016/S0022-4073(03)00146-8, 2003.

Sheese, P. E., Boone, C. D., and Walker, K. A.: Detecting physically unrealistic outliers in ACE-FTS atmospheric measurements, Atmos. Meas. Tech., 8, 741–750, doi:10.5194/amt-8-741-2015, 2015.

Stoew, B., Rieck, C., and Elgered, G.: First results from a new dual-channel water vapor radiometer, in: Proc. of the 14th Working Meeting on European VLBI for Geodesy and Astrometry, edited by: Tomasi, P., Mantovani, F., and Perez-Torres, M.-A., 79–82, http://www.evga.org/files/2000EVGA-proc_SanPietro.pdf (last access: 3 February 2016), 2000.

Straub, C., Espy, P. J., Hibbins, R. E., and Newnham, D. A.: Mesospheric CO above Troll station, Antarctica observed by a ground based microwave radiometer, Earth Syst. Sci. Data, 5, 199–208, doi:10.5194/essd-5-199-2013, 2013.

Ulich, B. L. and Haas, R. W.: Absolute calibration of millimeter-wavelength spectral lines, Astrophys. J. Suppl. Ser., 30, 247–258, doi:10.1086/190361, 1976.

Vassilev, V., Wadefalk, N., Kozhuharov, R., Abbasi, M., Gunnarsson, S. E., Zirath, H., Pellikka, T., Emrich, A., Pantaleev, M., Kallfass, I., and Leuther, A.: MMIC-Based Components for MM-Wave Instrumentation, IEEE Microwave Wireless Comp. Lett., 20, 578–580, doi:10.1109/LMWC.2010.2065797, 2010.

Waters, J., Wilson, W., and Shimabukuro, F.: Microwave measurement of mesospheric carbon monoxide, Science, 191, 1174, doi:10.1126/science.191.4232.1174, 1976.